OPTICS

Discovering the forbidden Raman modes at the edges of layered materials

Yao Guo[1,2], Weixuan Zhang[1], Hanchun Wu[1], Junfeng Han[1], Yongliang Zhang[2], Shenghuang Lin[2], Chunru Liu[2], Kang Xu[2], Jingsi Qiao[2,3], Wei Ji[3], Qing Chen[4], Song Gao[4], Wenjing Zhang[5], Xiangdong Zhang[1]*, Yang Chai[2]*

The edges of layered materials have unique properties that substantially differ from the body regions. In this work, we perform a systematic Raman study of the edges of various layered materials (MoS_2, WS_2, WSe_2, PtS_2, and black phosphorus). The Raman spectra of the edges feature newly observed forbidden Raman modes, which are originally undetectable from the body region. By selecting the edge type and the polarization directions of the incident and scattered light, all forbidden Raman modes are distinctly detected. Optical simulations show that the edges of layered materials drastically distort the electromagnetic fields of both the incident and scattered light, so that the light interacts with the edges in a distinct way, which differs from its interactions with the body regions.

INTRODUCTION

Through the interaction between light and matter, Raman spectroscopy provides abundant materials information, including light-electron-phonon interactions, interatomic coupling, strain, defects, doping, carrier mobility, thermal conductivity, chemical components, and chemical functionalization (1–6). Recently, a rich library of layered materials has drawn intense interest due to their unusual physical properties (7–10). Raman spectroscopy has been widely used to investigate layered materials (10–14). However, certain Raman-active modes of layered materials are undetectable with the commonly used Raman backscattering configuration. For example, 2H-phase group 6 transition metal dichalcogenides (TMDCs; such as MoS_2, WS_2, and WSe_2) have three Raman-active modes (E_{1g}, E_{2g}, and A_{1g}) in the high frequency range. In previous studies, the E_{2g} and A_{1g} modes have been well detected, while the E_{1g} mode is a forbidden Raman mode (11, 14). The E_{1g} mode is undetectable, unless a broken symmetry is introduced (15–17). Similarly, black phosphorus (BP) has six Raman-active modes, which are A_{1g}, B_{2g}, A_{2g}, B_{1g}, B^1_{3g}, and B^2_{3g}. Among these modes, only A_{1g}, B_{2g}, and A_{2g} are experimentally detectable. These three vibrational modes contain information about in-plane anisotropy, and they have been used to identify the lattice direction of BP (10). However, the other three Raman-active modes, B_{1g}, B^1_{3g}, and B^2_{3g} are forbidden and undetectable. These forbidden Raman modes have therefore been neglected in most previous studies and consequently bringing about incompleteness for the Raman spectroscopy of layered materials.

In addition, the terminal edges of layered materials exhibit unique magnetic, electronic, catalytic, topological, and optical properties that are in sharp contrast to those of the body region of the layered materials (18–23). However, there have been very few systematic Raman studies of the edges of layered materials (24, 25). In a recent study, two forbidden Raman modes of BP, B_{1g} and B^1_{3g}, were observed at the edges, and they were attributed to the presence of edge phonons (26). However, the mechanism underlying the Raman process in the edge region

needs to be verified by additional detailed experimental observations and analyses.

Here, we report on a systematic Raman study of the edges of various layered materials, including the 2H-phase MoS_2, WS_2, and WSe_2, the 1T-phase PtS_2, and BP. These experimental results demonstrate that all the forbidden Raman modes of layered materials (the E_{1g} mode of MoS_2, WS_2, and WSe_2 and the B_{1g}, B^1_{3g}, and B^2_{3g} modes of BP) can be selectively detected at the edges. We find that the selective detection of these forbidden modes depends upon the edge type, the polarization direction of the incident light, and the polarization direction of the scattered Raman signal. By combining analysis of the experimental results with simulations, we have constructed a comprehensive model that attributes the appearance of these forbidden Raman modes to the distortion of electromagnetic field in the edge region. Because of their unique refractive properties, the edges of layered materials drastically change the polarization and propagation direction of light, which enables the forbidden Raman modes to be detected. The principle underlying this work can be extended to other layered materials, and we expect it to contribute to a more comprehensive understanding of the optical properties of the edge regions of layered materials.

RESULTS

Raman spectra from the edge region of 2H-phase TMDCs

In this study, we investigated a variety of layered materials, including the 2H-phase MoS_2, WS_2, and WSe_2, the 1T-phase PtS_2, and BP. We mechanically exfoliated the layered material flakes from the bulk crystals onto a Si/SiO_2 substrate. We then collected microscopic Raman spectra from the exfoliated flakes using the common backscattering configuration, as shown schematically in Fig. 1A. First, we focus on the Raman modes of the 2H-phase MoS_2. Figure 1B shows a schematic diagram of the three Raman-active modes of 2H MoS_2: E_{1g}, E_{2g}, and A_{1g}. The signal intensities of the three Raman modes are shown in table S1. They are given by the Raman scattering formula $I = |e_i \cdot R \cdot e_s|^2$, where R is the Raman tensor, e_i is the polarization direction of the incident light, and e_s is the polarization direction of the scattered Raman signal. The E_{1g} mode is a forbidden Raman mode because its intensity is strictly zero. A more detailed discussion of the E_{1g} Raman mode is presented in section S2. The Raman spectra of MoS_2 from the body region and the edge region are collected and compared in Fig. 1C. The body region

[1]School of Physics, Beijing Institute of Technology, Beijing 100081, China. [2]Department of Applied Physics, The Hong Kong Polytechnic University, Hong Kong, China. [3]Department of Physics, Renmin University of China, Beijing 100872, China. [4]Key Laboratory for the Physics and Chemistry of Nanodevices, Department of Electronics, Peking University, Beijing 100871, China. [5]International Collaborative Laboratory of 2D Materials for Optoelectronics Science and Technology, Shenzhen University, Shenzhen 518060, China.
*Corresponding author. Email: zhangxd@bit.edu.cn (X.Z.); ychai@polyu.edu.hk (Y.C.)
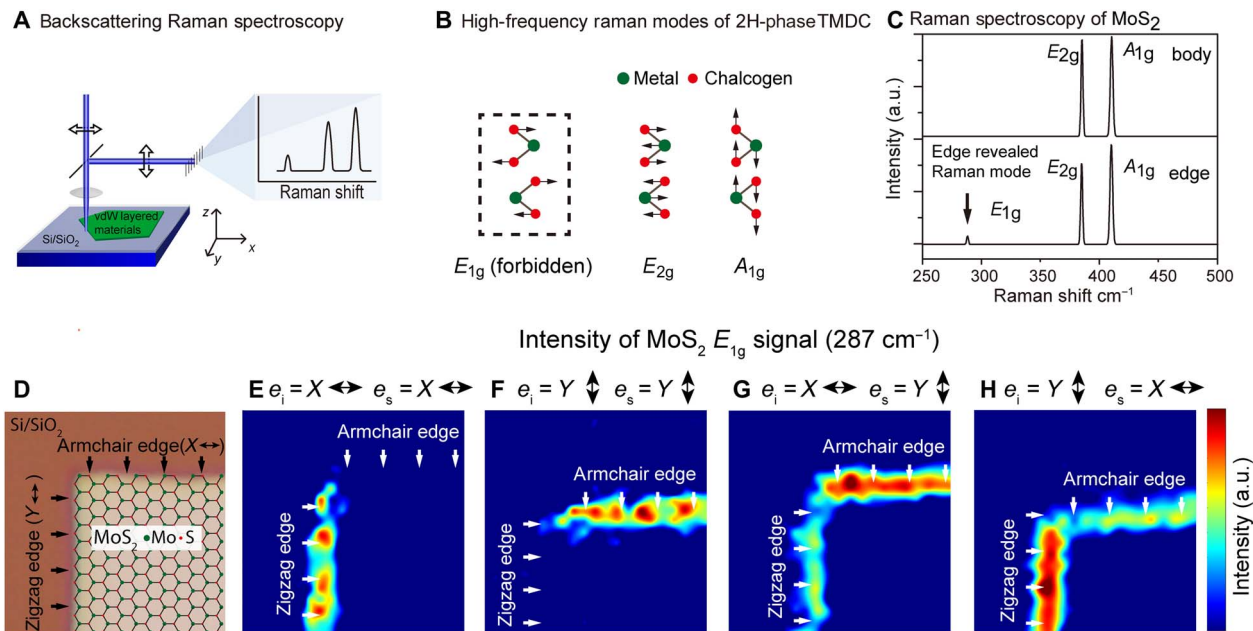
Fig. 1. Raman spectroscopy of MoS$_2$. (**A**) Schematic illustration of Raman backscattering spectroscopy. (**B**) Raman-active modes of 2H-phase TMDCs in the high frequency range. (**C**) Raman spectra of MoS$_2$ from the edge and from the body region. a.u., arbitrary units. (**D**) Optical image of a specific MoS$_2$ flake with the orthogonal armchair and zigzag edges. The intensity of E_{1g} signal is shown in (**E**) for [e_i, e_s] = [X, X], (**F**) for [e_i, e_s] = [Y, Y], (**G**) for [e_i, e_s] = [X, Y], and (**H**) for [e_i, e_s] = [Y, X]. The white arrows in (E) to (H) indicate the positions of the edges, corresponding to the black one-way arrows in (D).

exhibits only the E_{2g} and A_{1g} modes at 385 and 410 cm^{-1}. In sharp contrast, a new peak emerges in the Raman spectrum from the edge region. The position of the new peak exactly corresponds to the forbidden E_{1g} mode at 287 cm^{-1}. Although the intensity of the E_{1g} mode is less than 20% of the normal E_{2g} and A_{1g} modes, it is much higher than the noise level and is sufficiently distinct for further studies.

To obtain a fundamental understanding of the appearance of the E_{1g} mode, we further study its dependence on the edge type (zigzag or armchair), the polarization direction of the incident light (e_i), and that of the scattered Raman signal (e_s). Figure 1D shows the optical image of a specific MoS$_2$ flake with the orthogonal armchair and zigzag edges. The crystal orientation and the edge type of MoS$_2$ can be identified by a method reported in the recent literature (27). We designate the direction of the armchair edge as X and the direction of the zigzag edge as Y. The polarization directions of the incident light and the scattered Raman signal (e_i and e_s) are set along X or Y, respectively. By mapping the intensity of the E_{1g} mode, we find that for the armchair edge (X), the E_{1g} mode appears when [e_i, e_s] = [Y, Y] (Fig. 1F), [X, Y] (Fig. 1G), or [Y, X] (Fig. 1H), but it disappears when [e_i, e_s] = [X, X] (Fig. 1E). For the zigzag edge (Y), the E_{1g} mode appears when [e_i, e_s] = [X, X] (Fig. 1E), [X, Y] (Fig. 1G), or [Y, X] (Fig. 1H), but it disappears when [e_i, e_s] = [Y, Y] (Fig. 1F). Intensity maps of the E_{2g} and A_{1g} modes are shown in fig. S2. Detailed Raman spectra from the body region, the armchair edge, and the zigzag edge are shown in fig. S3, with [e_i, e_s] = [X, X], [Y, Y], [X, Y], and [Y, X]. Note that the peak position of the E_{1g} mode remains at 287 cm^{-1} for all the Raman spectra, with no red or blue shift, regardless of the edge type or the polarization directions e_i and e_s.

In a similar way, we studied the Raman spectra of the 2H-phase WS$_2$ and WSe$_2$, which have atomic structures and Raman modes identical to those of MoS$_2$. As shown in Fig. 2, we collected and compared the Raman spectra for WS$_2$ (Fig. 2, A to C) and WSe$_2$

(Fig. 2, D to F) from the body region, the armchair edge, and the zigzag edge. In Fig. 2A, the body region of WS$_2$ exhibits only the E_{2g} and A_{1g} modes at 356 and 421 cm^{-1}. Figure 2 (B and C) presents the Raman spectra of WS$_2$ from the armchair and zigzag edge regions. In contrast to the body region, the forbidden E_{1g} mode at 297 cm^{-1} appears at the armchair edges when [e_i, e_s] = [X, Y], [Y, X], or [Y, Y] (Fig. 2B) and at the zigzag edges when [e_i, e_s] = [X, X], [X, Y], or [Y, X] (Fig. 2C). For WSe$_2$, the Raman peak positions of E_{2g} and A_{1g} are 248 and 252 cm^{-1}, which are very close to each other. The intensity of the A_{1g} mode is much larger than that of the E_{2g} mode. As shown in Fig. 2D, the body region of WSe$_2$ shows only one merged peak when [e_i, e_s] = [X, X] or [Y, Y], which is dominated by the A_{1g} mode. When [e_i, e_s] = [X, Y] or [Y, X], the A_{1g} peak vanishes, and the E_{2g} peak emerges. Figure 2 (E and F) presents the Raman spectra of WSe$_2$ from the armchair and zigzag edge regions, respectively. The forbidden E_{1g} mode at 176 cm^{-1} appears at the armchair edges when [e_i, e_s] = [Y, Y], [X, Y], or [Y, X] (Fig. 2E) and at the zigzag edges when [e_i, e_s] = [X, X], [X, Y], or [Y, X] (Fig. 2F). Therefore, for MoS$_2$, WS$_2$, and WSe$_2$, the forbidden E_{1g} mode is detectable selectively at the edge regions, and the appearance of the E_{1g} peak depends on the edge type and the directions of e_i and e_s in the same way.

So far, we have obtained the forbidden E_{1g} peaks of MoS$_2$, WS$_2$, and WSe$_2$ from the edges. We find that the peak positions of the forbidden E_{1g} modes of 2H-phase TMDCs (Fig. 3) are correlated with those of the E_{2g} modes, as indicated by Eq. 1

$$\Delta_{E1g} : \Delta_{E2g} = \alpha(1 + 2m_{chal} : m_{metal})^{-1/2} \qquad (1)$$

where Δ_{E1g} and Δ_{E2g} are the shifts in the peak positions of the E_{1g} and E_{2g} modes, and m_{chal} and m_{metal} are the atomic masses of the chalcogenide and the metal in the TMDCs, respectively. We obtained the
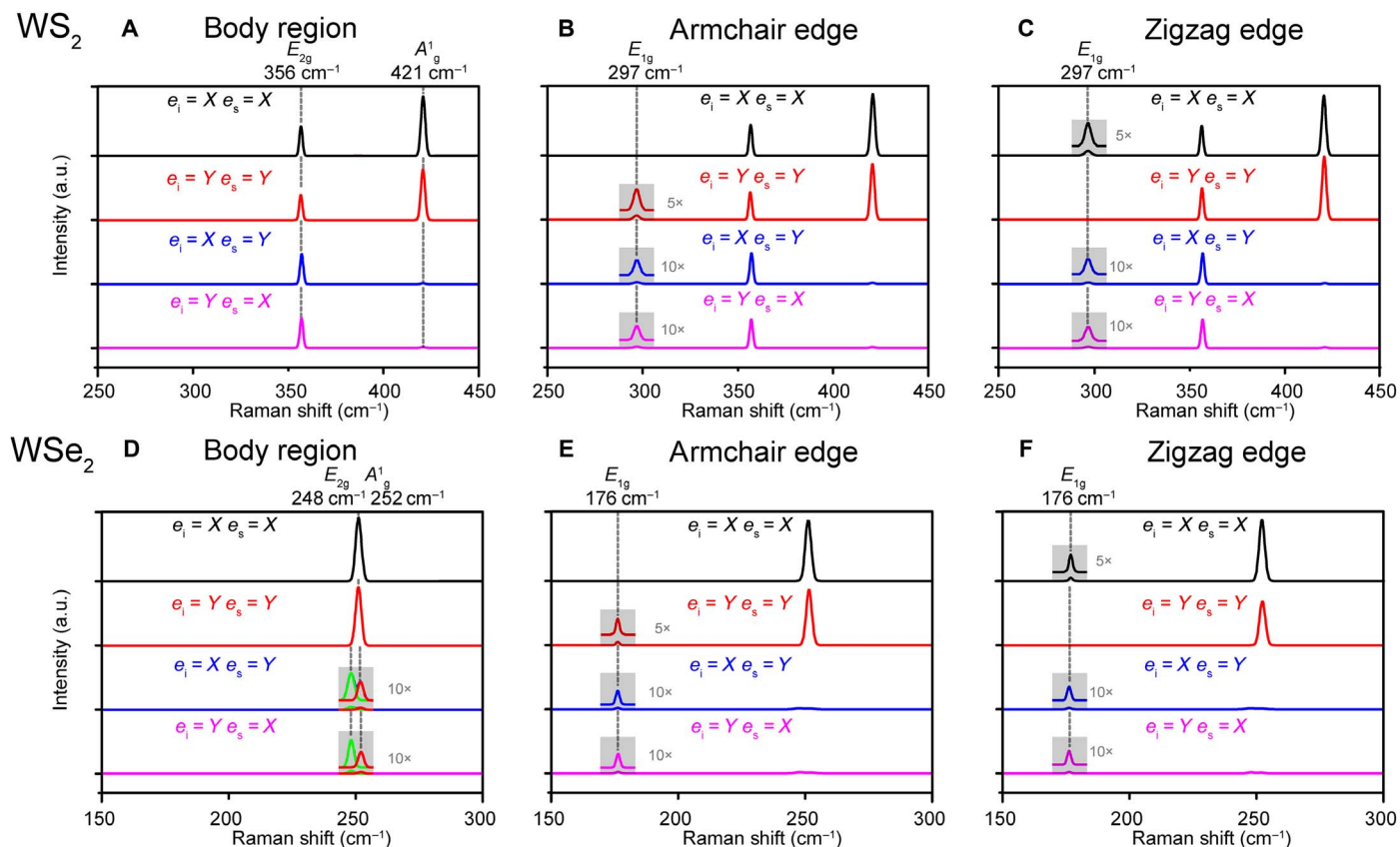
Fig. 2. Raman spectra of WS$_2$ and WSe$_2$. (**A** to **C**) Raman spectra of WS$_2$ from (A) the body region, (B) the armchair edge, and (C) the zigzag edge. (**D** to **F**) Raman spectra of WSe$_2$ from (D) the body region, (E) the armchair edge, and (F) the zigzag edge. The spectra vary with the polarization direction of the incident light e_i and the scattered Raman signal e_s (*X* or *Y*).
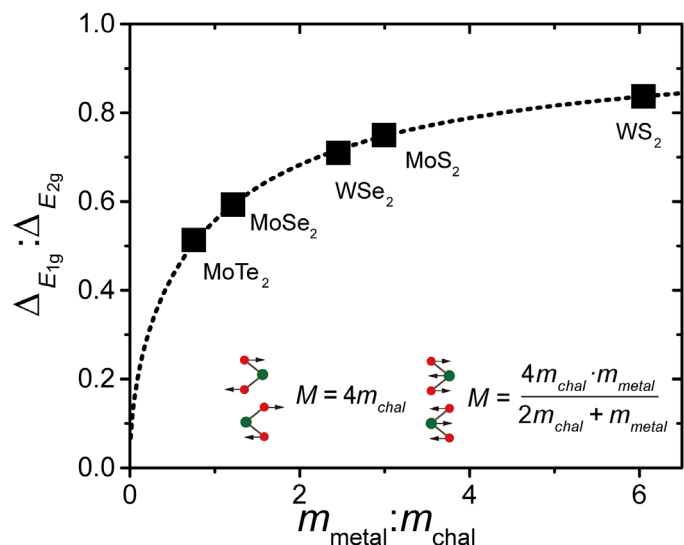
Fig. 3. Raman shift ratio of the E_{1g} and E_{2g} as a function of the atomic mass ratio in 2H-phase TMDCs.

Raman shifts of 2H-phase MoTe$_2$ and MoSe$_2$ from the literature (*16*, *17*). The fitting coefficient α is 0.966. The principle underlying Eq. 1 involves atomic lattice vibration dynamics. As illustrated in the inset in Fig. 3, for the E_{1g} phonons, only the chalcogenide atoms are involved, vibrating in

opposite directions, and the effective mass is $M_{E1g} = 4m_{chal}$. For the E_{2g} phonons, all the chalcogenide atoms vibrate in opposition to the metal atoms, and the effective mass is $M_{E2g} = 4m_{chal} \cdot m_{metal}/(2m_{chal} + m_{metal})$. The frequencies of the long-wavelength optical modes are given by

$$\omega_{E1g} = (2\beta_{E1g}/M_{E1g})^{-1/2}, \text{ and } \omega_{E2g} = (2\beta_{E2g}/M_{E2g})^{-1/2} \quad (2)$$

where ω_{E1g} and ω_{E2g} are the eigenfrequencies of the phonons, which are proportional to the Raman shifts. The quantities β_{E1g} and β_{E2g} are elastic constants, which are related to the interatomic interactions. With ω_{E1g}: $\omega_{E2g} = \Delta_{E1g}$: Δ_{E2g}, and inserting Eq. 2 into Eq. 1, we obtain β_{E1g}: $\beta_{E2g} = \alpha^2 = 0.932$. This result indicates that the relative vibration direction of the Janus chalcogenide atoms in the 2H-phase TMDCs makes a subtle difference to the interatomic interaction, whether in the opposite (E_{1g} mode) or the same (E_{2g} mode) direction.

Raman spectra from the edge region of BP

In addition to the forbidden Raman modes of MoS$_2$, WS$_2$, and WSe$_2$, we also investigated the Raman modes from the edge regions of BP. Figure 4A shows a BP flake with its orthogonal armchair and zigzag edges. As above, we denote the direction of the armchair edge as *X* and the direction of the zigzag edge as *Y*. The Raman-active modes of BP in the high frequency range are schematically illustrated in Fig. 4B. The intensities of the active modes of BP are calculated according to table S1. Among the six Raman-active modes, A_{1g}, B_{2g}, and A_{2g}
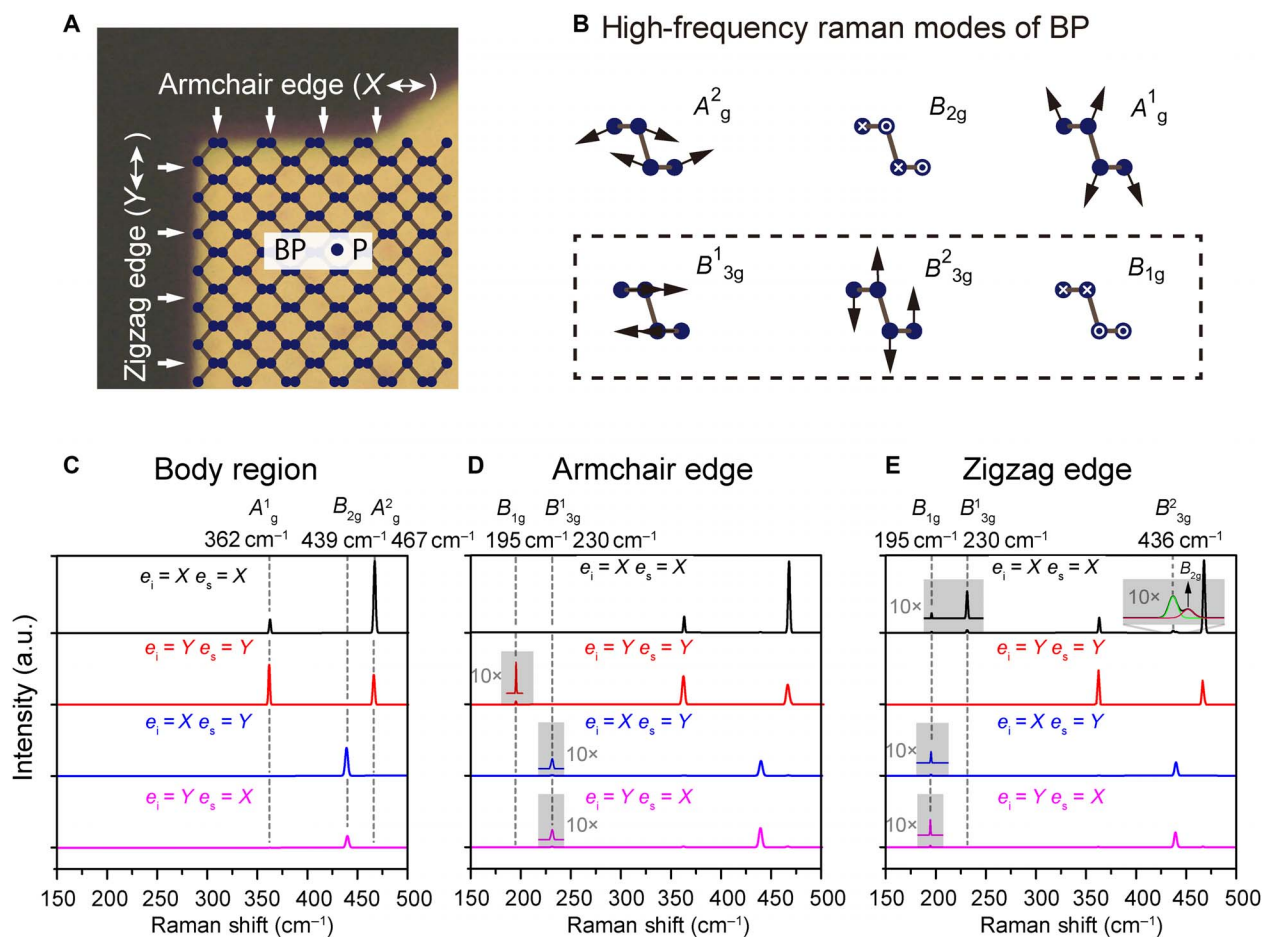
Fig. 4. Raman spectroscopy of BP. (**A**) Atomic structure and image of a BP flake with the orthogonal armchair edge and the zigzag edge. (**B**) Raman-active modes of BP in the high frequency range. (**C** to **E**) Raman spectra of BP from (C) the body region, (D) the armchair edge, and (E) the zigzag edge. The spectra vary with the polarization directions (X or Y) of the incident light e_i and the scattered Raman signal e_s.

are detectable, while B_{1g}, B^1_{3g}, and B^2_{3g} are forbidden. Figure 4C shows the Raman spectra from the body region of BP. The A_{1g}, B_{2g}, and A_{2g} are present at 362, 439, and 467 cm^{-1}, respectively, and their intensities vary as functions of e_i and e_s. We further collect the Raman spectra from the armchair edge of BP (Fig. 4D) and from the zigzag edge (Fig. 4E). The three forbidden Raman modes, B_{1g}, B^1_{3g}, and B^2_{3g}, appear in the edge regions. The B_{1g} peak, located at 195 cm^{-1}, appears at the armchair edge when $[e_i, e_s] = [Y, Y]$ (Fig. 4D) and at the zigzag edge when $[e_i, e_s] = [X, X]$, $[X, Y]$, or $[Y, X]$ (Fig. 4E). The B^1_{3g} peak, located at 230 cm^{-1}, appears at the armchair edge when $[e_i, e_s] = [X, Y]$ or $[Y, X]$ (Fig. 4D) and at the zigzag edges when $[e_i, e_s] = [X, X]$ (Fig. 4E). The peak position of the B^2_{3g} mode is 436 cm^{-1}, which is very close to the A_{2g} mode at 439 cm^{-1}. Thus, the peak of B^2_{3g} mode is submerged by the intense peak of A_{2g} mode when $[e_i, e_s] = [X, Y]$ or $[Y, X]$. The B^2_{3g} mode appears at the zigzag edge when $[e_i, e_s] = [X, X]$ (Fig. 4E), when the A_{2g} mode has almost vanished. Therefore, all the three forbidden Raman modes of BP are detected from the edge regions, depending upon the edge type and the directions of e_i and e_s.

Raman spectra of 1T-phase PtS₂

Last, we studied the Raman spectroscopy of 1T-phase PtS$_2$. PtS$_2$ has only two Raman-active modes in the high frequency range, which are E_{1g} and A_{1g} (28). Both modes are normal and unforbidden, with the

commonly used backscattering configuration, as shown in table S1. Raman spectroscopy from the edges of PtS$_2$ is identical to that from the body region. No new peaks besides the E_{1g} and A_{1g} modes emerge at the PtS$_2$ edges, as shown in fig. S4.

Theoretical modeling

We have demonstrated that the forbidden Raman modes of various layered materials, which are usually undetectable and have been neglected in previous work, can be selectively detected from the edge regions. A recent study has reported observations of the B_{1g} and B^1_{3g} modes from the BP edges. They attributed these forbidden modes to the presence of edge phonons (26). However, some experimental observations cannot be explained by this theory: (i) The frequency of edge phonon is sensitive to the atomic structures, while the new peaks at the zigzag edge and the armchair edge have the same peak positions. (ii) Edge phonons have a broad full width at half maximum (FWHM) because the reconstructed structure is close to an amorphous phase. However, the FWHM of the new peaks is as small as that of normal Raman peaks (a few cm^{-1}) from the crystalline body region. (iii) Edge phonons include multiple modes, while the new peaks correspond only to the forbidden Raman modes. A more detailed analysis is included in section S6. In the following discussion, we construct a model to explain the mechanism and provide an alternative explanation for the appearance of these forbidden Raman

modes. We focus on how the edges of layered materials distort the electromagnetic fields of both the incident light and the scattered Raman light, and we then derive a revised Raman intensity formula for the selective appearance of forbidden Raman modes at the edge region of layered materials.

Using the finite element method, we first simulate the incident light at the MoS_2 edge region. Figure 5 (A and B) shows the simulated electric field amplitudes and their components in the x, y, and z directions at the edge region, where the cross-profile is oriented along the xz plane and the edge direction is in the y direction. As a typical layered material, MoS_2 has anisotropic dielectric constants (or birefringent refractive indices). The in-plane and out-of-plane relative dielectric constants are $\varepsilon_{xy} = 20 + 15i$ and $\varepsilon_z = 4 + 0.3i$, respectively (29–31). In Fig. 5A, the incident light from the z direction is polarized in x, with $e_i = (1, 0, 0)$. The incident light is polarized perpendicular to the edge (y). Inside the MoS_2 edge region, the y-polarized component $|E_y|$ remains zero. The z-polarized component $|E_z|$ originates from the edge region to satisfy

the continuity boundary conditions for Maxwell's equations. Note that $|E_z|$ dominates the electric field in the edge region, rather than the original field $|E_x|$. The amplitude of $|E_z|$ is larger than that of $|E_x|$ because of the strong dielectric anisotropy of MoS_2. The real and imaginary parts of ε_{xy} are, respectively, 5 and 50 times larger than those of ε_z, indicating that the electric field in the x direction is mostly screened by polarization charges and damps quickly inside MoS_2. Therefore, the actual polarization direction of the incident light inside the edge region becomes $e_i^{edge} = (\delta_{ix}, 0, \delta_{iz})$, instead of the original $e_i = (1, 0, 0)$. By similar reasoning, for the cases in which the polarization direction of the incident light is orthogonal to the edge direction, i.e., (edge type = X, $e_i = Y$) or (edge type = Y, $e_i = X$), a z-polarized component $|E_z|$ arises, and a nonnegligible δ_{iz} must be included. In Fig. 5B, we further simulated the cases for which the polarization direction of the incident light is parallel to the edge direction. The incident light is set polarized in y. In contrast to the results shown in Fig. 5A, the polarization direction in this case remains unchanged inside the MoS_2. The components $|E_x|$ and $|E_z|$ remain zero,
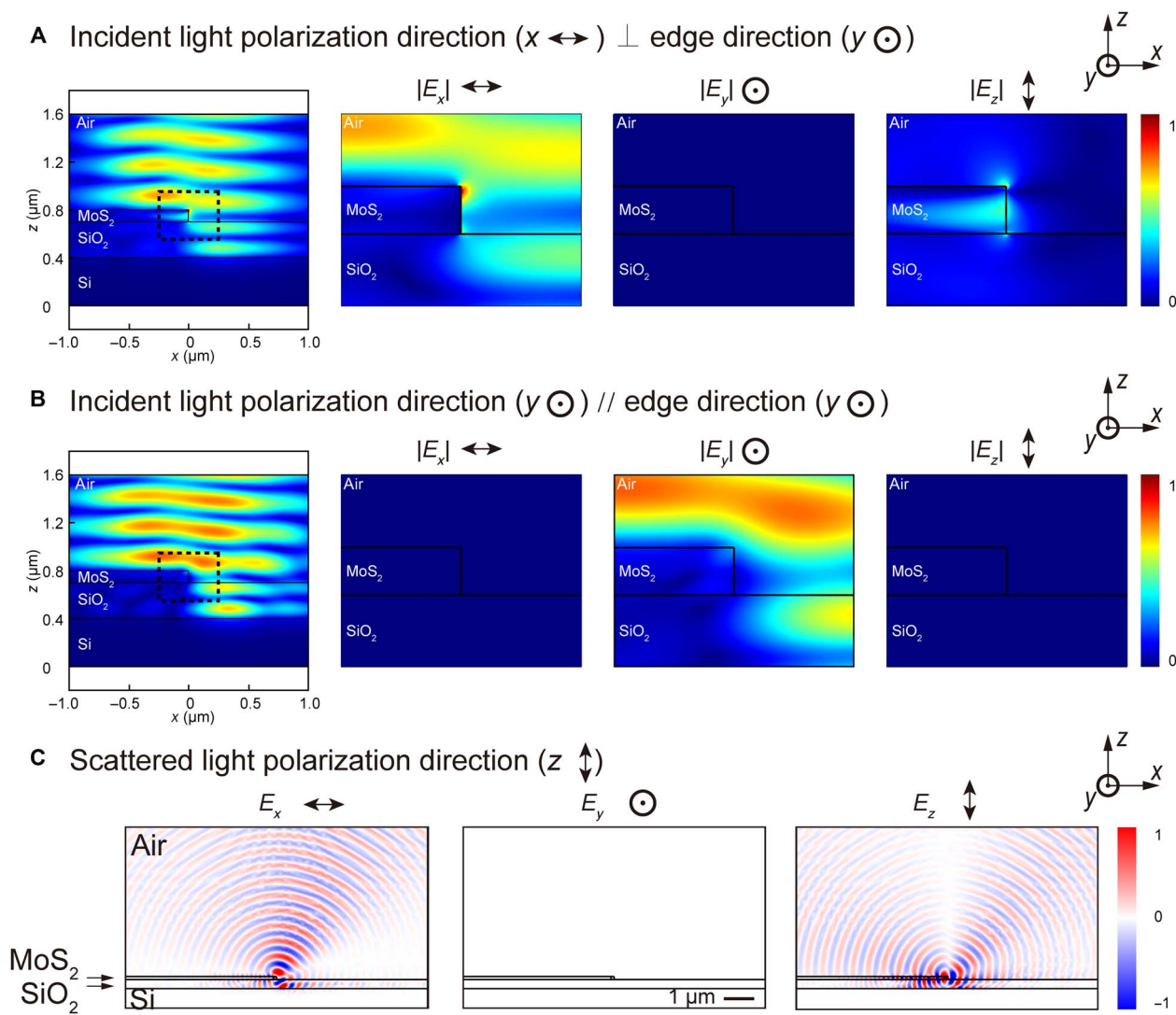
Fig. 5. Electric field of the incident light and the scattered Raman signal at the edge of a MoS_2 flake. The cross-profile is in the xz plane, with the edge direction along y. (**A**) The incident light from the z direction is polarized in the x direction with $e_i = (1, 0, 0)$. (**B**) The incident light from the z direction is polarized in y direction with $e_i = (0, 1, 0)$. The electric field amplitude is shown in (A) and (B). (**C**) Scattered Raman light with original polarization along z, a portion of the light propagates in the z direction with its polarization direction in x.

and the actual e_i^{edge} remains $(0, 1, 0)$. Therefore, in cases that the polarization direction of the incident light is parallel to the edge direction, i.e., (edge type = X, $e_i = X$) or (edge type = Y, $e_i = Y$), the electric field component of the incident light remains unchanged.

The presence of the edges distorts not only the incident light but also the scattered Raman light. In section S2, we have simulated the scattering of the E_{1g} signal from the body region of MoS₂. The incident light polarized in the xy plane generates E_{1g} signal polarized in the z direction. The z-polarized E_{1g} signal propagates along the xy plane and is soon reabsorbed by the MoS₂ itself. Thus, the E_{1g} signal cannot be collected and detected (see fig. S1). However, when the scattered E_{1g} signal meets a terminal edge, the direction of propagation is markedly changed. As shown in Fig. 5C, at the edge region, the electromagnetic field of the E_{1g} signal is distorted, and its propagation direction diverges at the edge. A portion of the E_{1g} signal propagates in the z direction with its polarization direction in x. Thus, the E_{1g} mode signal is detectable from the z direction, and the effective polarization direction e_s^{edge} becomes $(\delta_{sx}, 0, \delta_{sz})$, rather than the original $e_s = (1, 0, 0)$. Therefore, the edge changes the propagation direction of the Raman signal while keeping the polarization direction perpendicular to the edge. In the cases that (edge type = X, $e_s = Y$) and (edge type = Y, $e_s = X$), a non-negligible δ_{sz} must be included. While in the cases that the polarization direction of the scattered light is parallel to the edge direction, i.e., (edge type = X, $e_s = X$) or (edge type = Y, $e_s = Y$), the e_s remains unchanged.

From the above simulations, we see that the edges markedly distort the electromagnetic field of both the incident light and the scattered light. As a result, the intensities of the Raman modes, $I = |e_i \cdot R \cdot e_s|^2$, are modified to $I^{\text{edge}} = |e_i^{\text{edge}} \cdot R \cdot e_s^{\text{edge}}|^2$. The detailed calculation is given in section S7, and the updated expressions for I^{edge} of the forbidden Raman modes from the edges are listed in Table 1. We also develop the method to quantitatively compute I^{edge}, as shown in section S8. Similar analyses are applicable to the other layered materials studied in this work, including WS₂, WSe₂, and BP. Our theoretical model matches the experimental observations well. The forbidden Raman modes with nonzero I^{edge} are experimentally detected, depending upon the edge type and the polarization directions of incident and scattered light. A minor exception is the very weak B_{1g} peak observed at a zigzag edge (Y) with $[e_i, e_s] = [X, X]$. This may be due to the imaginary parts of the Raman tensor and the birefringence of BP, which have been reported to produce abnormal Raman responses (32, 33).

Similar analysis should also be applicable to other types of edge sites, such as the grain boundaries of polycrystalline layered materials, where the refractive index may also change across the edge sites, as described in detail in section S9. We also recognize the forbidden Raman modes detected from the powder and dispersion samples (fig. S9), which possibly relate to the edge sites to a certain degree. In addition to Raman scattering, the principle of this model is also applicable to other light-matter interactions, such as photoluminescence, Rayleigh scattering, and high-order harmonic generations.

DISCUSSION

In summary, we have demonstrated that all the forbidden Raman modes of layered materials (E_{1g} of 2H-phase MoS₂, WS₂, and WSe₂ and B_{1g}, B^1_{3g}, and B^2_{3g} of BP) are detectable from the edges. The selective detection of these forbidden Raman modes depends upon the edge types and the polarization directions of the incident light and scattered Raman signals. We have constructed a comprehensive model to clarify the underlying mechanism, which is related to the markedly distorted

Table 1. Calculated expression of I^{edge} for the forbidden Raman modes. Correspondingly, a "yes" indicates that the mode is experimentally detected, while a "no" indicates that the mode is not experimentally detected. N/A, not applicable.

E_{1g} mode of MoS₂, WS₂, and WSe₂		$[e_i, e_s]$			
		$[X, X]$	$[Y, Y]$	$[X, Y]$	$[Y, X]$
Armchair (X)	I^{edge}	0	$d^2(\delta_{iz}^2\delta_{sy}^2 + \delta_{iy}^2\delta_{sz}^2)$	$d^2\delta_{sz}^2$	$d^2\delta_{iz}^2$
	Detected	No	Yes	Yes	Yes
Zigzag (Y)	I^{edge}	$d^2(\delta_{iz}^2\delta_{sx}^2 + \delta_{ix}^2\delta_{sz}^2)$	0	$d^2\delta_{iz}^2$	$d^2\delta_{sz}^2$
	Detected	Yes	No	Yes	Yes
B_{1g} of BP		$[X, X]$	$[Y, Y]$	$[X, Y]$	$[Y, X]$
Armchair (X)	I^{edge}	0	$h^2(\delta_{iz}^2\delta_{sy}^2 + \delta_{iy}^2\delta_{sz}^2)$	0	0
	Detected	No	Yes	No	No
Zigzag (Y)	I^{edge}	0	0	$h^2\delta_{iz}^2$	$h^2\delta_{sz}^2$
	Detected	Yes (weak)	No	Yes	Yes
B^1_{3g} of BP		$[X, X]$	$[Y, Y]$	$[X, Y]$	$[Y, X]$
Armchair (X)	I^{edge}	0	0	$i^2\delta_{sz}^2$	$i^2\delta_{iz}^2$
	Detected	No	0	Yes	Yes
Zigzag (Y)	I^{edge}	$i^2(\delta_{iz}^2\delta_{sx}^2 + \delta_{ix}^2\delta_{sz}^2)$	0	0	0
	Detected	Yes	No	No	No
B^2_{3g} of BP		$[X, X]$	$[Y, Y]$	$[X, Y]$	$[Y, X]$
Armchair (X)	I^{edge}	0	0	$j^2\delta_{sz}^2$	$j^2\delta_{iz}^2$
	Detected	No	No	N/A	N/A
Zigzag (Y)	I^{edge}	$j^2(\delta_{iz}^2\delta_{sx}^2 + \delta_{ix}^2\delta_{sz}^2)$	0	0	0
	Detected	Yes	No	N/A	N/A

electromagnetic fields at the layered material/air interfaces. We expect this work to provide a method for probing the forbidden Raman modes of layered materials, contribute to a more complete comprehension of Raman spectroscopy, and inspire a more detailed research on the unique optical properties of the edge regions of layer materials.

MATERIALS AND METHODS
Material preparation
MoS₂, WS₂, WSe₂, PtS₂, and BP flakes were obtained by exfoliating the bulk samples onto 300-nm SiO₂/Si substrates. The thickness of the flakes was measured by the atomic force microscope (MoS₂, 56 nm; WS₂, 47 nm; WSe₂, 148 nm; PtS₂, 248 nm; BP, 106 nm). For layered

material flakes thinner than 30 nm, we were not able to experimentally detect the forbidden Raman modes.

Raman characterization

Raman spectroscopy was conducted using a 488-nm laser as the incident light, with a spot size of ~1.5 μm. We tuned the polarization direction of the incident light with a half-wave plate. We collected the scattered Raman light with a 50× lens with a numerical aperture of 0.55, and we selected the polarization direction with a polarizer plate. We performed two-dimensional mapping with a step size of 0.5 μm.

SUPPLEMENTARY MATERIALS

Supplementary material for this article is available at http://advances.sciencemag.org/cgi/content/full/4/12/eaau6252/DC1

Section S1. Raman tensors of MoS_2, WS_2, WSe_2, BP, and PtS_2 (high frequency range)
Section S2. Scattering of the E_{1g} mode from the body region
Section S3. Intensity maps of the MoS_2, E_{2g}, and A_{1g} peaks
Section S4. Raman spectra of MoS_2 from the body region, the armchair edge, and the zigzag edge
Section S5. Raman modes and spectra of PtS_2
Section S6. Analysis on the edge phonons
Section S7. Calculation of $I^{edge} = |e_i^{edge} \cdot R \cdot e_s^{edge}|^2$
Section S8. Quantitative computation of I^{edge}
Section S9. Raman spectra in other types of edge sites
Section S10. Raman spectra from the MoS_2 powder and dispersion samples
Table S1. Raman tensors and intensity expressions of layered materials at high frequency range.
Fig. S1. Cross-sectional image of the electromagnetic field of the E_{1g} Raman signal.
Fig. S2. Intensity maps of the MoS_2 E_{2g}, and A_{1g} peaks.
Fig. S3. Raman spectra of MoS_2.
Fig. S4. Raman spectra of PtS_2.
Fig. S5. Simulated edge phonon modes in the range of 260 to 300 cm^{-1}.
Fig. S6. Computation of the forbidden Raman mode intensity at the edge region.
Fig. S7. Electric field component of incident light and scattered Raman signal at the edge site of polycrystalline BP.
Fig. S8. Incident light, scattered Raman light, and Raman spectra from edge sites where thickness changes.
Fig. S9. Raman spectra from powder and dispersion samples.
References (34–40)

REFERENCES AND NOTES

1. D. A. Long, D. Long, *Raman Spectroscopy* (McGraw-Hill, 1977).
2. N. Colthup, *Introduction to Infrared and Raman spectroscopy* (Elsevier, 2012).
3. H. J. Bowley, D. L. Gerrard, J. D. Louden, G. Turrell, D. J. Gardiner, P. R. Graves, *Practical Raman spectroscopy* (Springer Science & Business Media, 2012).
4. A. C. Ferrari, D. M. Basko, Raman spectroscopy as a versatile tool for studying the properties of graphene. *Nat. Nanotechnol.* **8**, 235–246 (2013).
5. K. Kneipp, H. Kneipp, I. Itzkan, R. R. Dasari, M. S. Feld, Ultrasensitive chemical analysis by Raman spectroscopy. *Chem. Rev.* **99**, 2957–2976 (1999).
6. E. Yalon, C. J. McClellan, K. K. H. Smithe, M. Muñoz Rojo, R. L. Xu, S. V. Suryavanshi, A. J. Gabourie, C. M. Neumann, F. Xiong, A. B. Farimani, E. Pop, Energy dissipation in monolayer MoS_2 electronics. *Nano Lett.* **17**, 3429–3433 (2017).
7. D. N. Basov, M. M. Fogler, F. J. García de Abajo, Polaritons in van der Waals materials. *Science* **354**, aag1992 (2016).
8. K. S. Novoselov, A. Mishchenko, A. Carvalho, A. H. C. Neto, 2D materials and van der Waals heterostructures. *Science* **353**, aac9439 (2016).
9. S. Das, J. A. Robinson, M. Dubey, H. Terrones, M. Terrones, Beyond graphene: Progress in novel two-dimensional materials and van der Waals solids. *Ann. Rev. Mater. Res.* **45**, 1–27 (2015).
10. F. Xia, H. Wang, Y. Jia, Rediscovering black phosphorus as an anisotropic layered material for optoelectronics and electronics. *Nat. Commun.* **5**, 4458 (2014).
11. H. Li, Q. Zhang, C. C. R. Yap, B. K. Tay, T. H. T. Edwin, A. Olivier, D. Baillargeat, From bulk to monolayer MoS_2: Evolution of Raman scattering. *Adv. Funct. Mater.* **22**, 1385–1390 (2012).
12. X. Zhang, X.-F. Qiao, W. Shi, J.-B. Wu, D.-S. Jiang, P.-H. Tan, Phonon and Raman scattering of two-dimensional transition metal dichalcogenides from monolayer, multilayer to bulk material. *Chem. Soc. Rev.* **44**, 2757–2785 (2015).
13. K. Gołasa, M. Grzeszczyk, R. Bożek, P. Leszczyński, A. Wysmołek, M. Potemski, A. Babiński, Resonant Raman scattering in MoS_2—From bulk to monolayer. *Solid State Commun.* **197**, 53–56 (2014).
14. C. Lee, H. Yan, L. E. Brus, T. F. Heinz, J. Hone, S. Ryu, Anomalous lattice vibrations of single- and few-layer MoS_2. *ACS Nano* **4**, 2695–2700 (2010).
15. N. Scheuschner, R. Gillen, M. Staiger, J. Maultzsch, Interlayer resonant Raman modes in few-layer MoS_2. *Phys. Rev. B* **91**, 235409 (2015).
16. D. Nam, J.-U. Lee, H. Cheong, Excitation energy dependent Raman spectrum of $MoSe_2$. *Sci. Rep.* **5**, 17113 (2015).
17. G. Froehlicher, E. Lorchat, F. Fernique, C. Joshi, A. Molina-Sánchez, L. Wirtz, S. Berciaud, Unified description of the optical phonon modes in *N*-layer $MoTe_2$. *Nano Lett.* **15**, 6481–6489 (2015).
18. Y.-W. Son, M. L. Cohen, S. G. Louie, Half-metallic graphene nanoribbons. *Nature* **444**, 347 (2006).
19. H. I. Karunadasa, E. Montalvo, Y. Sun, M. Majda, J. R. Long, C. J. Chang, A molecular MoS_2 edge site mimic for catalytic hydrogen generation. *Science* **335**, 698–702 (2012).
20. X. Yin, Z. Ye, D. A. Chenet, Y. Ye, K. O'Brien, J. C. Hone, X. Zhang, Edge nonlinear optics on a MoS_2 atomic monolayer. *Science* **344**, 488–490 (2014).
21. Y. Guo, J. Yin, X. Wei, Z. Tan, J. Shu, B. Liu, Y. Zeng, S. Gao, H. Peng, Z. Liu, Q. Chen, Edge-states-induced disruption to the energy band alignment at thickness-modulated molybdenum sulfide junctions. *Adv. Electron. Mater.* **2**, 1600048 (2016).
22. C. Zhang, Y. Chen, J.-K. Huang, X. Wu, L.-J. Li, W. Yao, J. Tersoff, C.-K. Shih, Visualizing band offsets and edge states in bilayer–monolayer transition metal dichalcogenides lateral heterojunction. *Nat. Commun.* **7**, 10349 (2016).
23. S. Tang, C. Zhang, D. Wong, Z. Pedramrazi, H.-Z. Tsai, C. Jia, B. Moritz, M. Claassen, H. Ryu, S. Kahn, J. Jiang, H. Yan, M. Hashimoto, D. Lu, R. G. Moore, C.-C. Hwang, C. Hwang, Z. Hussain, Y. Chen, M. M. Ugeda, Z. Liu, X. Xie, T. P. Devereaux, M. F. Crommie, S.-K. Mo, Z.-X. Shen, Quantum spin Hall state in monolayer 1T'-WTe₂. *Nat. Phys.* **13**, 683 (2017).
24. L. G. Cançado, M. A. Pimenta, B. R. A. Neves, M. S. S. Dantas, A. Jorio, Influence of the atomic structure on the Raman spectra of graphite edges. *Phys. Rev. Lett.* **93**, 247401 (2004).
25. Z. Liu, M. Amani, S. Najmaei, Q. Xu, X. Zou, W. Zhou, T. Yu, C. Qiu, A. G. Birdwell, F. J. Crowne, R. Vajtai, B. I. Yakobson, Z. Xia, M. Dubey, P. M. Ajayan, J. Lou, Strain and structure heterogeneity in MoS_2 atomic layers grown by chemical vapour deposition. *Nat. Commun.* **5**, 5246 (2014).
26. H. B. Ribeiro, C. E. P. Villegas, D. A. Bahamon, D. Muraca, A. H. Castro Neto, E. A. T. de Souza, A. R. Rocha, M. A. Pimenta, C. J. S. de Matos, Edge phonons in black phosphorus. *Nat. Commun.* **7**, 12191 (2016).
27. Y. Guo, C. Liu, Q. Yin, C. Wei, S. Lin, T. B. Hoffman, Y. Zhao, J. Edgar, Q. Chen, S. P. Lau, J. Dai, H. Yao, H.-S. P. Wong, Y. Chai, Distinctive in-plane cleavage behaviors of two-dimensional layered materials. *ACS Nano* **10**, 8980–8988 (2016).
28. Y. Zhao, J. Qiao, P. Yu, Z. Hu, Z. Lin, S. P. Lau, Z. Liu, W. Ji, Y. Chai, Extraordinarily strong interlayer interaction in 2D layered PtS_2. *Adv. Mater.* **28**, 2399–2407 (2016).
29. W. Wang, X. Cui, E. Yang, Q. Fan, B. Xiang, Negative refraction in molybdenum disulfide. *Opt. Express* **23**, 22024–22033 (2015).
30. H. Zhang, Y. Ma, Y. Wan, X. Rong, Z. Xie, W. Wang, L. Dai, Measuring the refractive Index of highly crystalline monolayer MoS_2 with high confidence. *Sci. Rep.* **5**, 8440 (2015).
31. X. Yan, L. Zhu, Y. Zhou, Y. E, L. Wang, X. Xu, Dielectric property of MoS_2 crystal in terahertz and visible regions. *Appl. Opt.* **54**, 6732–6736 (2015).
32. H. B. Ribeiro, M. A. Pimenta, C. J. S. de Matos, R. L. Moreira, A. S. Rodin, J. D. Zapata, E. A. T. de Souza, A. H. Castro Neto, Unusual angular dependence of the Raman response in black phosphorus. *ACS Nano* **9**, 4270–4276 (2015).
33. N. Mao, J. Wu, B. Han, J. Lin, L. Tong, J. Zhang, Birefringence-directed Raman selection rules in 2D black phosphorus crystals. *Small* **12**, 2627–2633 (2016).
34. G. Benedek, W. Kress, F. W. de Wette, J. E. Black, V. Celli, W. Kress, A. A. Maradudin, L. Miglio, D. L. Mills, G. I. Stegeman, *Surface Phonons* (Springer Berlin Heidelberg, 2013).
35. G. P. Srivastava, *The Physics of Phonons* (Taylor & Francis, 1990).
36. Y. Li, Z. Hu, S. Lin, S. K. Lai, W. Ji, S. P. Lau, Giant anisotropic Raman response of encapsulated ultrathin black phosphorus by uniaxial strain. *Adv. Funct. Mater.* **27**, 1600986 (2016).
37. L. Liang, J. Wang, W. Lin, B. G. Sumpter, V. Meunier, M. Pan, Electronic bandgap and edge reconstruction in phosphorene materials. *Nano Lett.* **14**, 6400–6406 (2014).
38. D. Le, T. S. Rahman, Joined edges in MoS_2: Metallic and half-metallic wires. *J. Phys. Condens. Matter* **25**, 312201 (2013).
39. V. Dzhagan, A. G. Milekhin, M. Y. Valakh, S. Pedetti, M. Tessier, B. Dubertret, D. R. T. Zahn, Morphology-induced phonon spectra of CdSe/CdS nanoplatelets: Core/shell *vs.* core-crown. *Nanoscale* **8**, 17204–17212 (2016).
40. N. Driza, S. Blanco-Canosa, M. Bakr, S. Soltan, M. Khalid, L. Mustafa, K. Kawashima, G. Christiani, H. U. Habermeier, G. Khaliullin, C. Ulrich, M. Le Tacon, B. Keimer, Long-range transfer of electron–phonon coupling in oxide superlattices. *Nat. Mater.* **11**, 675–681 (2012).

Citation: Y. Guo, W. Zhang, H. Wu, J. Han, Y. Zhang, S. Lin, C. Liu, K. Xu, J. Qiao, W. Ji, Q. Chen, S. Gao, W. Zhang, X. Zhang, Y. Chai, Discovering the forbidden Raman modes at the edges of layered materials. *Sci. Adv.* **4**, eaau6252 (2018).